Supplementary Information (SI)

Highly stable linking platinum and porous spinel via carbon bridge engineering towards long-lifespan of rechargeable zinc-air battery

Mei Wang,*[a] Hao Du,[a] Yong Nian,[a] Guanshui Ma,[b] Jinfang Zhang,[a] Xiaoguang Wang*[c] and Xiaofeng Li*[a]

[a] School of Materials Science and Engineering, North University of China, Taiyuan 030051, China

[b] State Key Laboratory of Advanced Marine Materials, Zhejiang Key Laboratory of Extreme environmental Material Surfaces and Interfaces, Ningbo Institute of Materials Technology and Engineering, Chinese Academy of Sciences, Ningbo 315201, China

[c] Laboratory of Advanced Materials and Energy Electrochemistry, School of Materials Science and Engineering, Taiyuan University of Technology, Taiyuan 030024, China

* Corresponding author: wangmei@nuc.edu.cn, wangxiaoguang@tyut.edu.cn, lxf@nuc.edu.cn

1. Experimental section

Physicochemical characterizations. The phase characterizations were conducted on X-ray diffraction (XRD, DX-2700BH, China) with a Cu Kα radiation source (λ=0.154 nm) at 40 kV and 30 mA. Operando XRD measurements were performed on the same diffractometer at 40 kV and 40 mA using the in situ XRD cell (Beijing Science Star Technology Co.Ltd. China), which was filled with continuously circulating electrolyte. Raman spectra were recorded by a Renishaw Qontor with an excitation wavelength of 532 nm. In situ Raman spectra were obtained by equipping with an in-situ Raman cell (Beijing Science Star Technology Co.Ltd. China), which taken glassy carbon as working electrode, Ag/AgCl as reference electrode and platinum wire as counter electrode. Prior to recording Raman signals, the chronoamperometry curves were run at the varied potentials in the range of 1.0 to 0.2 V. Fourier transform infrared (FTIR) was conducted with the device of BRUKER ALPHA II to verify the newborn functional groups during synthesis or electrochemical testing. The microtopography and element mappings were acquired by scanning electron microscopy (SEM, JSM-7900F, Japan) and its build-in energy dispersive spectrometer (EDS). Transmission electron microscope (TEM) images were obtained on JEM-2010F. The high-angle annular dark-field (HAADF) imaging in an aberration-corrected scanning transmission electron microscope (STEM, JEM-ARM300F (Grand ARM)) was used to characterize the atomic structure. Brunauer-Emmet-Teller (BET) curves were measured on BSD-PS2. Inductively coupled plasma (ICP) was detected on Vista Axial CCD (Varian) and tested at least three times for each sample. The chemical valence states of superficial elements were analyzed via X-ray photoelectron spectroscopy (XPS, ESCALAB 250Xi, America) with an Al anode. X-ray absorption fine structure (XAFS) was measured at the easyXAFS150 station (easyXAFS, LLC, USA), which was employed to track the valence state and coordination geometry of Pt sites.

Electrocatalytic OER/ORR measurements. The OER and ORR activities were assessed by electrochemical workstation (CS2350H, China) linked with RRDE-3A and three-electrode system, of which glassy carbon electrode (GCE) supported by catalyst inks, platinum wire/carbon rod and Ag/AgCl served as working electrode, counter electrode and reference electrode, respectively. The working electrode was integrated by mixing 4 mg catalyst powder and 1 mg carbon black (Vulcan XC-72) into 100 μL Nafion solution (0.5 wt.%) and 300 μL isopropanol as well as forming a homogeneous

ink. Then, dropping 5 μL catalyst onto a pre-polished GCE (Φ=5mm) and spontaneously drying under at room temperature to get working electrode. Theoretically speaking, Pt loading quantity during electro-catalysis is 0.032 mg cm^{-2}. In the process of electrochemical measurement, the electrolyte for OER and ORR were 1 M KOH (pH=14) and O_2-saturated 0.1 M KOH (pH=13), respectively. And all potentials involved in the two reactions should be transformed into reversible hydrogen electrode (RHE) according to the following equation:

$$E_{RHE} = E_{Ag/AgCl} + 0.197 + 0.059 \times \mathrm{pH} \quad \text{(S1)}$$

The potentials measured from linear sweep voltammetry (LSV) curves should be corrected by 5% iR_s due to the effect of solution resistance (R_s). To obtain overpotential (η) of OER, the potential should be further subtracted equilibrium potential (1.23 V). To make clear dynamic mechanism of ORR, it's necessary to firstly test LSV curves at various rotation speeds (400-2500 rpm) and then convert them to K-L curves. Finally, based on the following equations, the electron transfer number *n* can be calculated.

$$\frac{1}{j} = \frac{1}{j_K} + \frac{1}{j_d} \quad \text{(S2)}$$

$$j_d = 0.2nFAD^{\frac{2}{3}}v^{-\frac{1}{6}}C\omega^{\frac{1}{2}} \quad \text{(S3)}$$

$$\omega = 2\pi f/60 \quad \text{(S4)}$$

where j, j_k and j_d are the measured current, kinetic restrained current and diffusion restrained current. F, A, D, *v* and C represent Faraday constant (96485 C mol^{-1}), surface area of rotating disk electrode (0.19625 cm^2), diffusivity of oxygen (1.9×10^{-5} cm^2 s^{-1}), dynamic viscosity of 0.1 M KOH (0.01 cm^2 s^{-1}) and concentration of dissolved oxygen (1.2×10^{-3} mol L^{-1}), respectively. ω (rad/s) is angular speed, which can be transformed from rotation speed (rpm) via formula (4).

The rotating ring-disk electrode (RRDE) with Pt ring (A_r = 0.1884 cm^2) and glassy carbon disk (A_d = 0.1256 cm^2) was used to determine the selectivity of four-electron. According to formula (5) and (6), the values of *n* and H_2O_2 yield during the whole potential range of ORR can be accurately calculated.

$$n = 4 \times \frac{I_d}{I_d + I_r/N} \quad \text{(S5)}$$

$$H_2O_2(\%) = 200 \times \frac{I_r/N}{I_d + I_r/N} \quad \text{(S6)}$$

where N is the current collection efficiency of RRDE (N=0.424), and I_d and I_r are the disk current and ring current, respectively.

The Tafel slopes were converted from LSV by utilizing the following equation:

$$\eta = b \times log|j| + a \quad \text{(S7)}$$

where η and j were overpotential and current density, respectively, which can be acquired from LSV. As well as Tafel slope (b) can be calculated when Tafel constant (a) was given.

Electrochemical surface area (ECSA) reflected the intrinsic property of catalyst and could be reckoned from the value of double-layer capacitance (C_{dl}) based on the following equation:

$$ECSA = \frac{C_{dl}}{Cs} = \frac{C_{dl}}{40\mu cm^{-2} per\ cm^{2}_{ECSA}} \quad \text{(S8)}$$

where C_s is the specific capacitance of a flat surface that could be in the range of 20～60 μF cm^{-2}, and 40 μF cm^{-2} is chosen as a moderate value in this study as previous literatures did [1].

Zn-air battery measurements. The RZABs were assembled with commercial Zn plate as anode, Pt/np-CFO@C or Pt/C loaded carbon paper as cathode and mixed solution (6M KOH + 0.2M $Zn(Ac)_2$) as electrolyte. Thereinto, the cathode should reload a current collector and a gas diffusion layer as well as rolling them together. To decrease concentration polarization and speed up reaction kinetics, an external pump-started circulatory system was introduced to simultaneously keep the electrolyte fresh (Fig. S4a). Specific capacity (mAh g^{-1}) of RZAB represents the amount of charge that can be discharged per unit mass of the electrode material and can be calculated by the following equation:

$$Specific\ capacity = \frac{j \times t}{m_{Zn}} \quad \text{(S9)}$$

where *j* is applied current density, *t* is discharge-servicing time and m_{Zn} is the mass of Zn consumed.

Energy density (mWh g^{-1}/Wh kg^{-1}) of RZAB represents the amount of energy stored per unit mass and can be calculated by the following equation:

$$Energy\ density = U \times Specific\ capacity \quad \text{(S10)}$$

where U is average voltage of discharge.

Theoretical simulation. All theoretical simulation were performed by density

functional theory (DFT) using the Vienna ab initio simulation package (VASP). The exchange-correlation energy can be dealt with Perdew-Burke-Ernzerhof (PBE) functional. The projected augmented wave (PAW) pseudopotentials were used to depict the electron-ion interaction. The vacuum layer thickness was set as 15 Å to avoid interference between adjacent slabs. Then, all the computations were running with a cutoff energy of 400 eV, while the convergence precision for ion steps and self-consistent field were set to be 0.03 eV $Å^{-1}$ and 10^{-5} eV, respectively. The Brillouin zones were sampled by a 2×2×1 k-point grid.

Generally, alkaline ORR can be divided into the following four steps [2]:

$$* + O_2 + H_2O + e^- \rightarrow *OOH + OH^- \quad \text{(S11)}$$

$$*OOH + e^- \rightarrow *O + OH^- \quad \text{(S12)}$$

$$*O + H_2O + e^- \rightarrow *OH + OH^- \quad \text{(S13)}$$

$$*OH + e^- \rightarrow * + OH^- \quad \text{(S14)}$$

where *, *OOH, *O and *OH represent clean catalyst, catalyst adsorbed with intermediates OOH, O and OH, respectively. Accordingly, the Gibbs free energy (G) of intermediate adsorption model can be calculated by the following formula:

$$G = E + E_{ZPE} - TS \quad \text{(S15)}$$

where E and E_{ZPE} describe the total energy and zero-point energy, respectively. T and S represent temperature and entropy, respectively. Afterwards, the Gibbs free energy difference (ΔG) of the four elementary reactions can be computed by the following formula [3]:

$$\Delta G_1 = G(*OOH) - G(*) - G(O_2) - G(H_2O) + G(OH^-) \quad \text{(S16)}$$

$$\Delta G_2 = G(*O) - G(*OOH) + G(OH^-) \quad \text{(S17)}$$

$$\Delta G_3 = G(*OH) - G(*O) - G(H_2O) + G(OH^-) \quad \text{(S18)}$$

$$\Delta G_4 = -1.6 - \Delta G_1 - \Delta G_2 - \Delta G_3 \quad \text{(S19)}$$

As for OER, the intermediate steps are opposite to those of ORR, but the RDS decision rules are same to those of ORR.

2. Supplemental Fig.s and tables

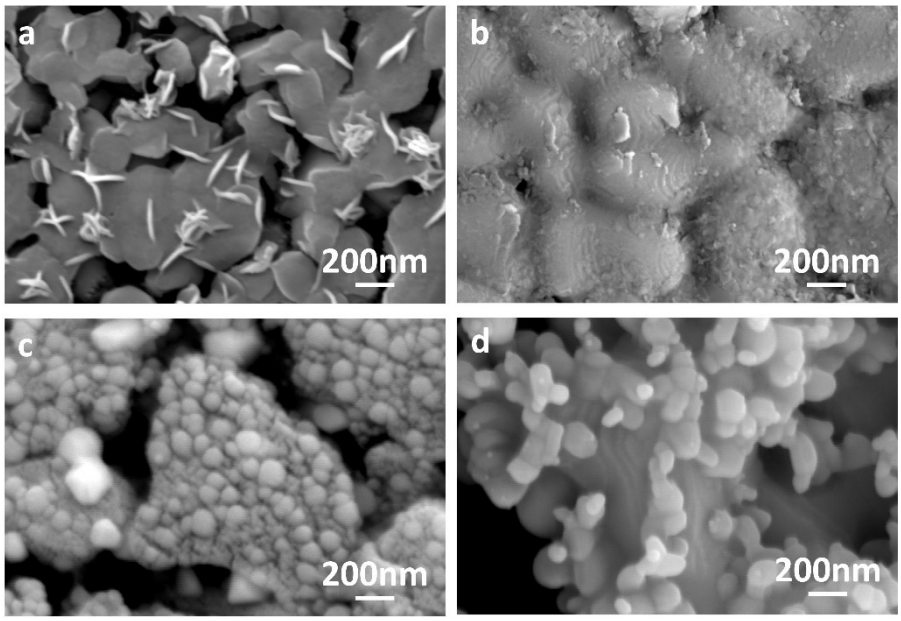

Fig. S1 SEM images of (a) np-CFO, (b) np-CFO@C, (c) Pt/np-CFO@C, (d) Pt/np-CFO.

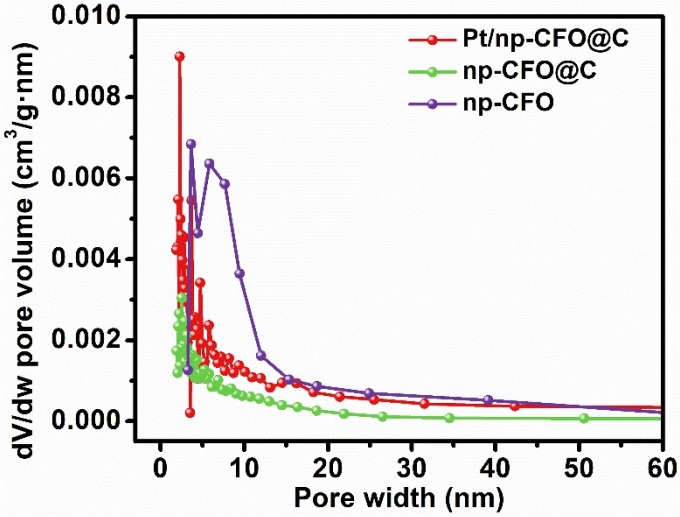

Fig. S2 Pore size distribution of np-CFO, np-CFO@C and Pt/np-CFO@C electrodes.

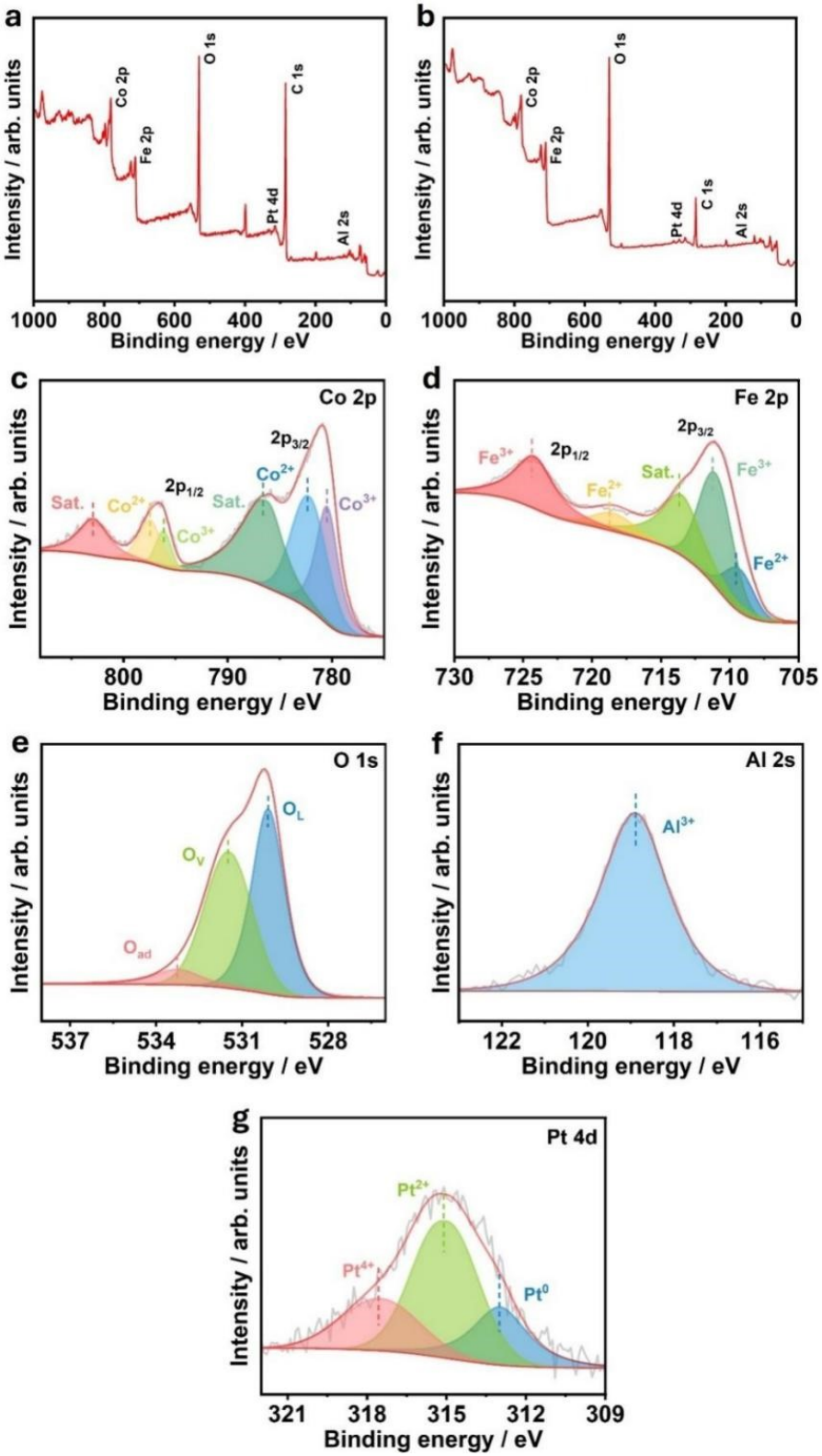

Fig. S3 XPS full scan of Pt/np-CFO@C electrode. XPS spectra of Pt/np-CFO electrode: (b) full scan, (c) Co 2p, (d) Fe 2p, (e) O 1s, (f) Al 2s and (g) Pt 4d.

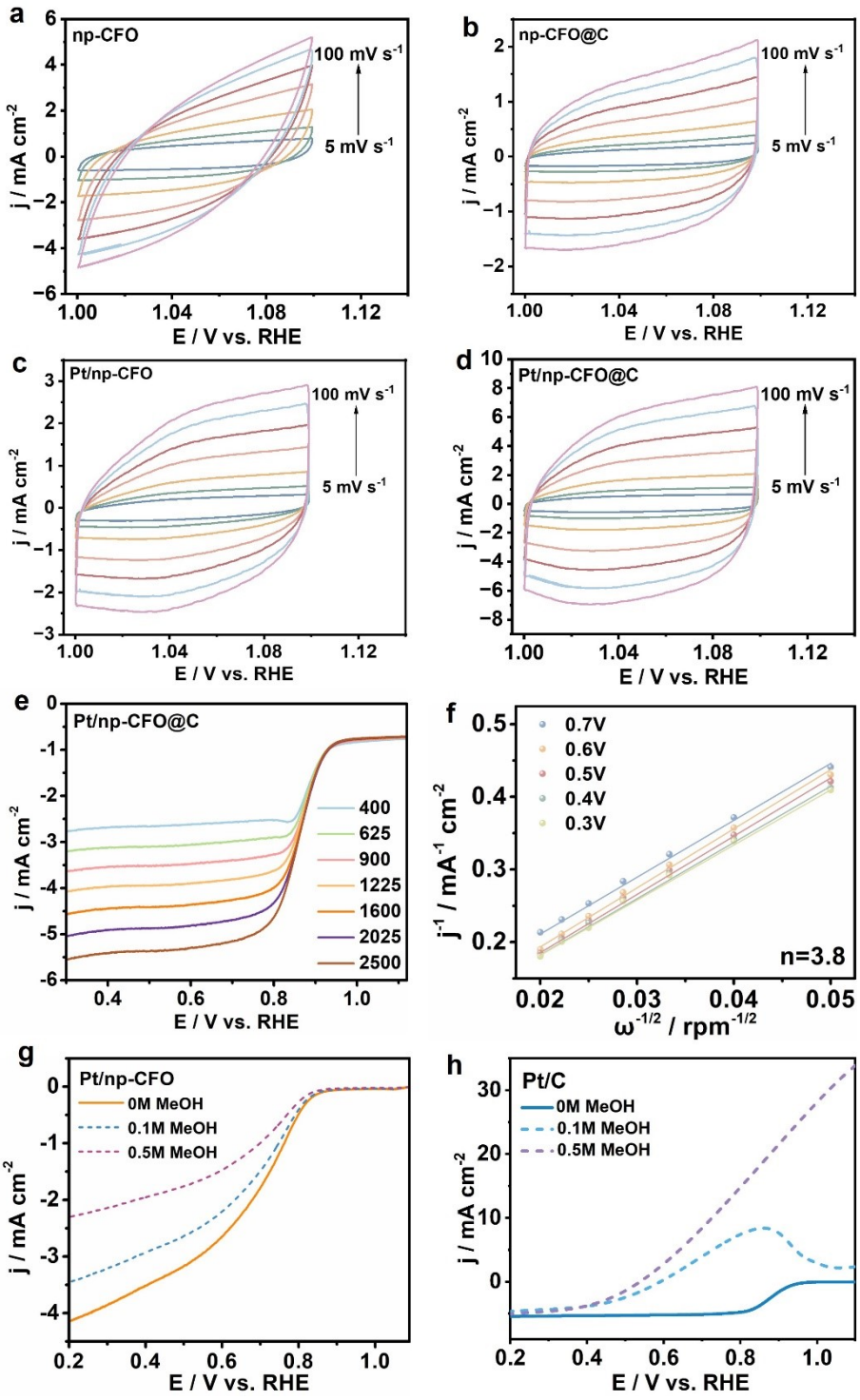

Fig. S4 CV curves (1.0～1.1 V vs. RHE) of (a) np-CFO, (b) np-CFO@C, (c) Pt/np-CFO and (d) Pt/np-CFO@C electrodes under different scan rates. (e) ORR polarization curves of Pt/np-CFO@C at various rotation rates. (f) K-L curves at different potentials. (g) Methanol tolerance of Pt/np-CFO. (h) Methanol tolerance of Pt/C.

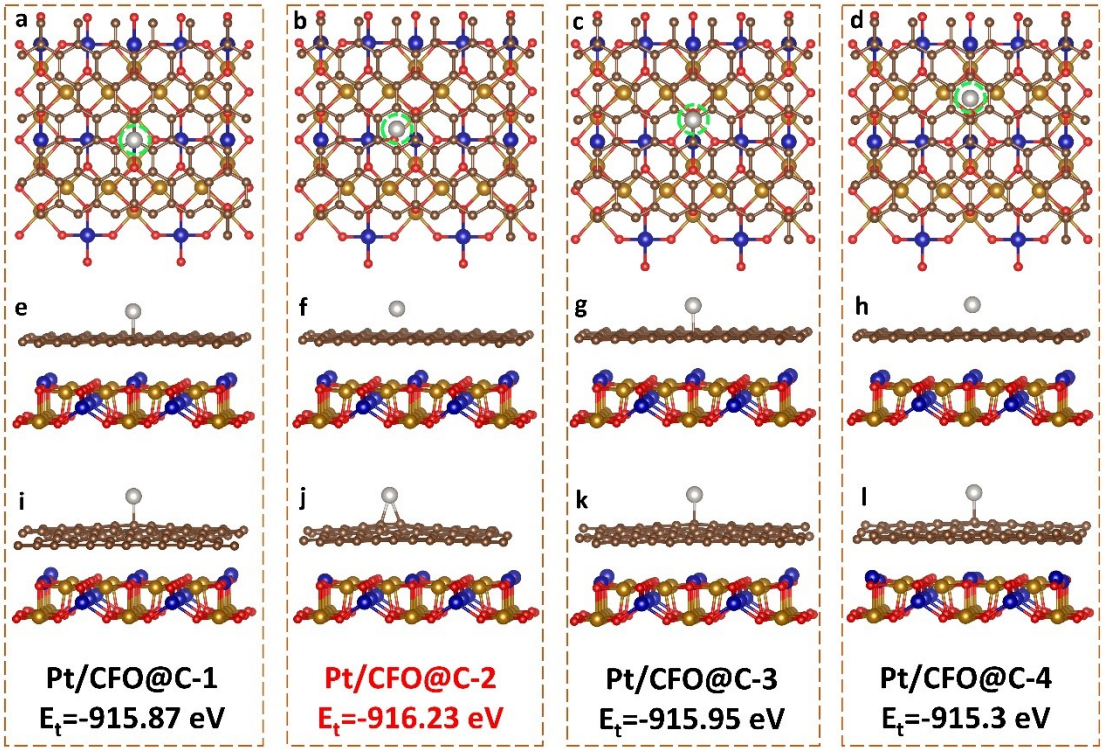

Fig. S5 (a-d) Pt-loading models of CFO@C on different sites. (e-h) Side views before optimizing. (i-l) Side views after optimizing.

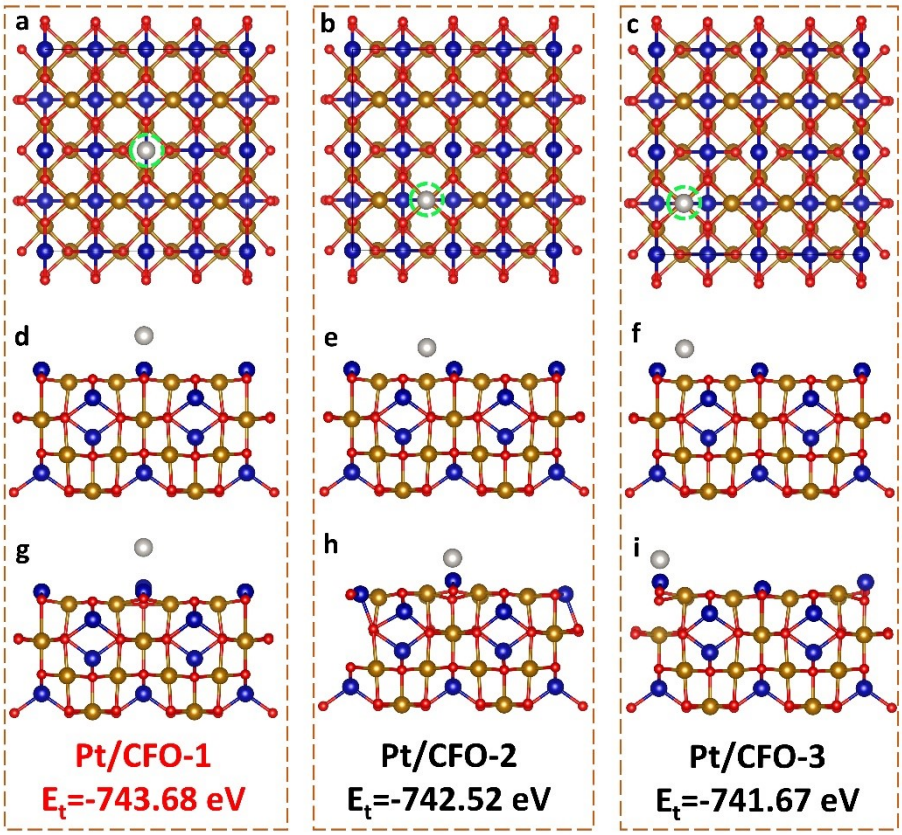

Fig. S6 (a-c) Pt-loading models of CFO on different sites. (d-f) Side views before optimizing. (g-i) Side views after optimizing.

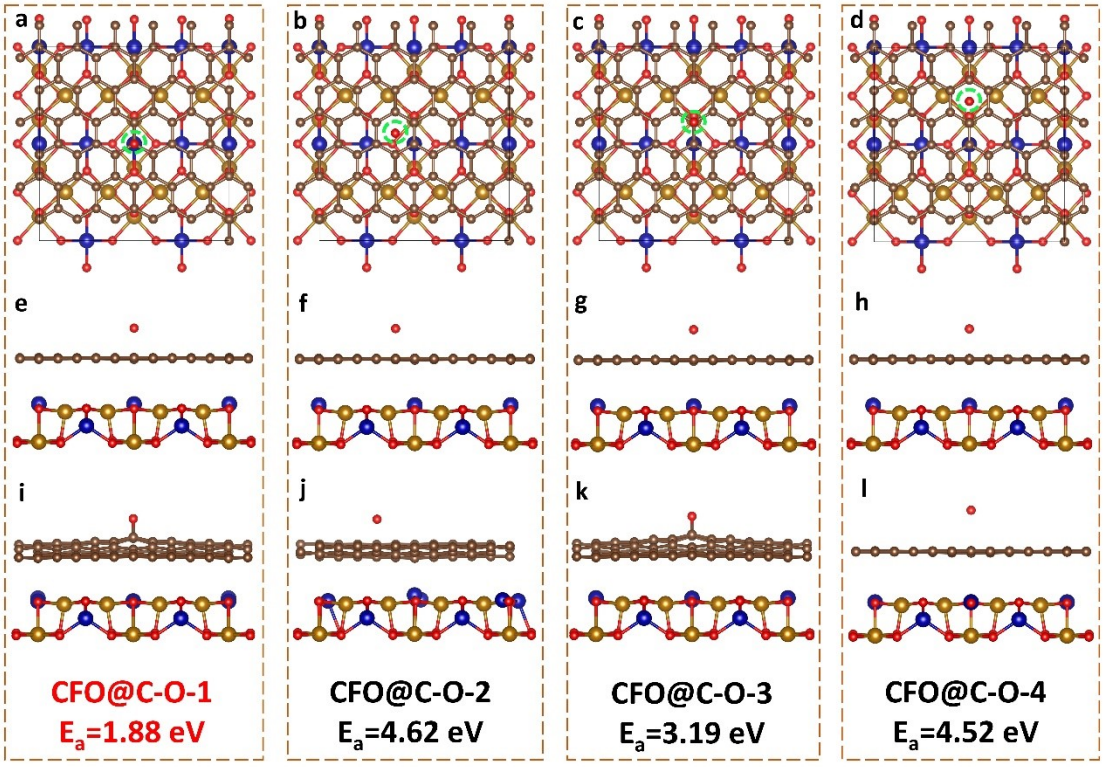

Fig. S7 (a-d) *O adsorption models of CFO@C on different metal sites. (e-h) Side views before optimizing. (i-l) Side views after optimizing.

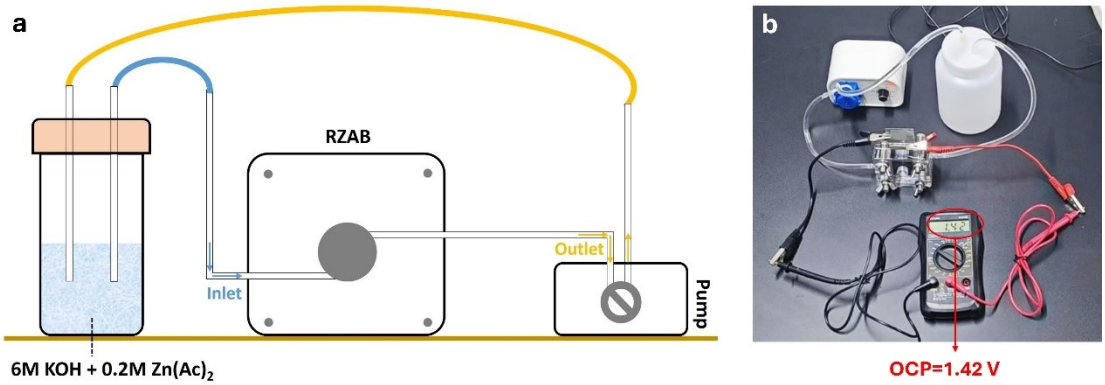

Fig. S8 (a) Schematic of liquid RZAB drived by circulating pump. (b) Open-circuit voltage of Pt/np-CFO@C based RZAB measured by multimeter.

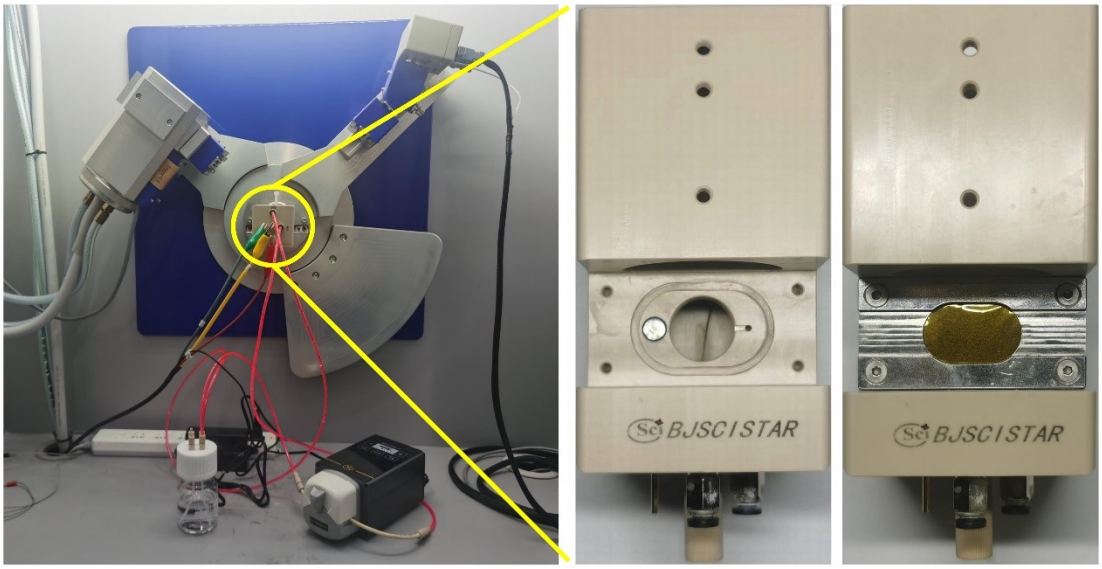

Fig. S9 Optical photograph of in-situ XRD applied to a liquid RZAB.

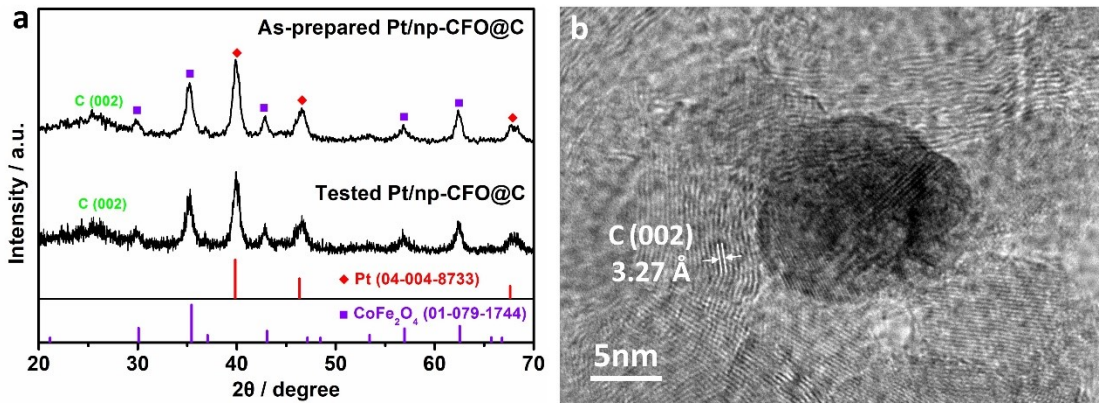

Fig. S10 (a) XRD patterns of as-prepared Pt/np-CFO@C and tested Pt/np-CFO@C. (b) HRTEM image of Pt/np-CFO@C after in-situ XRD testing.

Table S1. ICP analysis of Pt/np-CFO@C and Pt/np-CFO.

Catalysts	(Sample quality m=0.05 g, Constant volume V=10mL)			
	Al / wt. %	**Co / wt. %**	**Fe / wt. %**	**Pt / wt. %**
Pt/np-CFO@C	0.68	6.48	12.98	5.09
Pt/np-CFO	2.33	19.51	36.02	4.45

Table S2. XPS peak area ratio of Pt^0, Pt^{2+} and Pt^{4+} for Pt/np-CFO@C and Pt/np-CFO.

	Pt^0	**Pt^{2+}**	**Pt^{4+}**
Pt/np-CFO@C	35.22%	28.28%	36.50%
Pt/np-CFO	21.75%	53.85%	24.40%

Table S3. Electrochemical impedance parameters obtained by fitting the Nyquist plots of Pt/np-CFO@C, np-CFO@C, Pt/np-CFO and np-CFO to the equivalent circuit mode.

Catalysts	R_s / Ω	R_{ct} / Ω
Pt/np-CFO@C	1.46	37.2
np-CFO@C	1.67	67.7
Pt/np-CFO	2.52	10.5
np-CFO	1.33	172.9

Table S4. Comparison of the electrochemical OER activities of this work with recent outstanding reported electrocatalysts in 1M KOH.

Electrocatalyst	η_{10} (mV)	Tafel slope (mV dec^{-1})	Reference
Pt/np-CFO@C	**329**	**79.8**	
np-CFO@C	**333**	**148.9**	
Pt/np-CFO	**403**	**73.2**	**This work**
np-CFO	**320**	**126.7**	
RuO_2	**312**	**124.7**	
Pt@$Ti_3C_2T_x$-rGO	490	165.32	[4]
Pt-V_S@TaSSe	390	--	[5]
(Ni, Fe, Pt)-N-C	371	--	[6]
3%Pt/NiW/NF	344		[7]
PtCo/G-2h	339	58	[8]
Co-Pt@Fe-N-C	410	171.25	[9]

Table S5. Comparison of the electrochemical ORR activities of this work with recent outstanding reported electrocatalysts in 0.1M KOH.

Electrocatalyst	$E_{1/2}$ (V)	j_L (mA cm^{-2})	Tafel slope (mV dec^{-1})	Reference
Pt/np-CFO@C	**0.86**	**5.69**	**65.4**	
np-CFO@C	**0.75**	**4.96**	**91.9**	
Pt/np-CFO	**0.67**	**4.15**	**112.5**	**This work**
np-CFO	**0.47**	**3.37**	**219.05**	
Pt/C	**0.85**	**5.41**	**85.6**	
Pt_3Rh-Co_3O_4	0.75	--	83	[10]
Pt/PMx	0.825	4.35	76	[11]
Pt/$Ti_3C_2T_x$	0.801	--	114.75	[12]
PtCoCN(CDs-0.10)	0.83	4.58	64.6	[13]
Pt/NiFe-LDH@ Co_9S_8	0.83	--	92	[14]

Table S6. RZAB activities of Pt/np-CFO@C ‖ Pt/np-CFO@C couple along with other reported catalysts.

Couple	OCV (V)	Power density (mW cm^{-2})	Cycling time (h)	Reference
Pt/np-CFO@C	**1.42**	**185.45**	**1400**	**This work**
PtCo/NC	--	109.8	--	15
PtFeCoNiMnGa/CNT	1.52	130.6	120	16
Pt/NiFe-LDH@ Co_9S_8	1.47	164.3	1050	14
PtSn/NC	1.41	150.1	120	17
PBO CO_2@A-N	1.41	128.1	--	18
Pt/NiFe-LDH	1.44	30	1300	19
(Ni, Fe, Pt)-N-C	1.4	175	300	6
Co-Pt@Fe-N-C	1.52	151	850	9
Pt@ZIF-8/Pt-12	1.48	120.8	600	20

References

1 M. Wang, W. Zhang, F. Zhang, Z. Zhang, B. Tang, J. Li and X. Wang, *ACS Catal.,* 2019, **9**, 1489-1502.

2 Q. Wang, Y. Gong, X. Zi, L. Gan, E. Pensa, Y. Liu, Y. Xiao, H. Li, K. Liu, J. Fu, J. Liu, A. Stefancu, C. Cai, S. Chen, S. Zhang, Y. R. Lu, T. S. Chan, C. Ma, X. Cao, E. Cortes and M. Liu, *Angew. Chem. Int. Edit.,* 2024, e202405438.

3 Q. Zhou, C. Xu, J. Hou, W. Ma, T. Jian, S. Yan and H. Liu, *Nano-Micro Lett.,* 2023, **15**, 95.

4 L. Vazhayal, S. B. Alex and S. K. Haram, *J. Mater. Chem. A,* 2024, **12**, 27671-27685.

5 X. Yang, L. Lin, X. Guo and S. Zhang, *Small,* 2024, **20**, 2404000.

6 M. Liu, Z. Zhang, Y. Zhang, Z. Zhao, B. Liu, F. Kong, A. Chen, L. Zhao and Z. Wang, *Electrochim. Acta,* 2025, **541**, 147323.

7 H. K. Basak, M. K. Adak, A. Rajput and B. Chakraborty, *ACS Appl. Mater. Interfaces,* 2025, **17**, 9391-9406.

8 L. Qiang, X. Yang, H. Xiao, P. Zhao, Q. Yan, W. Wen, C. Liu, Q. Guo, Y. Zhang, M. Zhao and J. Jia, *Int. J. Hydrogen Energy,* 2025, **155**, 150356.

9 J. Yang, S. Song, Z. Chen, B. Zhang, Y. Guo, Y. Guo and H. Zhang, *J. Mater. Chem. A,* 2025, **13**, 6020-6026.

10 N. Bhuvanendran, C. W. Park, H. Su and S. Y. Lee, *Environ. Res.,* 2023, **229**, 115950.

11 R. S. Mane, H. M. Wilson, B. N. Patil, S. J. Lee and N. Jha, *J. Mater. Chem. A,* 2025, DOI: 10.1039/d5ta04239a.

12 S. B. Alex, L. Vazhayal, P. P. Waghmaitar, R. R. Urkude, B. B. Chandashive, D. Khushalani and S. K. Haram, *ACS Appl. Energy Mater.,* 2024, **7**, 1890-1901.

13 L. Yang, J. Ma, Y. Liu, C. Ma, X. Yu and Z. Chen, *Nanoscale,* 2024,

16, 5433-5440.

14 J. Chen, Z. Liu, Y. Liu, Z. Cheng, J. Zhang, Q. Zhang, Y. Li, C. Hou, K. Li and H. Wang, *Energy Fuels,* 2024, **38**, 10264-10274.

15 M. Zhang, T. Zhou, D. Bukhvalov, F. Han, C. Wang and X. Yang, *Appl. Catal. B-Environ.,* 2023, **337**, 122976.

16 L. Luo, R. Tang, L. Su, J. Kou, X. Guo, Y. Li, X. Cao, J. Cui and S. Gong, *Energy Storage Mater.,* 2024, **72**, 103773.

17 B. Li, J. Liu, C. Zhao, A. Hu, X. Sun, B. Mei and J. Long, *Inorg. Chem.,* 2024, **63**, 19322-19331.

18 T. Zhang, L. Meng, J. Ren, N. Wang, L. Du, X. Zhang, L. Xing, C. Tang and S. Ye, *Mater. Today Energy,* 2025, **53**, 101985.

19 M. Nie, D. Liu, Z. Fu, X. Li and Y. Zhang, *Chem. Commun.,* 2025, DOI: 10.1039/d5cc04360c.

20 Y. Chen, W. Sun, J. Yao, Z. Yang, Q. Wang, C. Xu, G. Ren, Z. Liu and X. Liu, *J. Mater. Sci.,* 2025, ***60***, 2786-2803.